

## ABSTRACT

Title of Thesis: DETERMINATION OF METHODS TO EFFECTIVELY STUDY INTERFACES IN SODIUM SOLID STATE BATTERIES

Mary Rose York, Master of Science, 2021

Thesis Directed By: Prof. Paul Albertus, Department of Chemical & Biomolecular Engineering

As countries across the globe pledge to decrease their carbon footprint, the demand for sustainable resources has grown drastically. An increase in the energy density of electrochemical energy storage devices would advance the use of low-carbon electrical energy sources. Successful implementation of a metallic anode may allow for this increase; however, alkali metal electrodes are hindered by their reactive nature and instability at the electrode-electrolyte interface. These challenges extend to both liquid and solid electrolytes, though integration of solid electrolytes shows promise of obtaining higher energy batteries. The solid metal electrode-solid electrolyte interface is largely unexplored, but we have determined that the application of stack pressure allows for increased cyclability in all solid-state cells. Further, it is of utmost importance to achieve a pristine interface through heat treatment and polishing procedures. Data found in the literature is difficult to

compare; thus, careful reporting of experimental conditions is important to efficient advancement of research.

DETERMINATION OF METHODS TO STUDY INTERFACES IN SODIUM  
SOLID STATE BATTERIES

by

Mary Rose York

Thesis submitted to the Faculty of the Graduate School of the  
University of Maryland, College Park, in partial fulfillment  
of the requirements for the degree of  
Master of Science  
2021

Advisory Committee:  
Prof. Paul Albertus, Chair  
Prof. Eric Wachsman  
Prof. Po-Yen Chen

© Copyright by  
Mary Rose York  
2021

## Dedication

I dedicate this thesis to my mother. Thank you for being my number one cheerleader – always supportive and constantly encouraging me to succeed. Without you, I would not be who I am today.

## Acknowledgements

I would like to first acknowledge and thank my advisor, Dr. Paul Albertus for giving me invaluable guidance over the last few years. Second, I would like to thank my committee members: Dr. Eric Wachsman and Dr. Po-Yen Chen; I am grateful the time they have taken to sit on my thesis committee.

I'd like to thank my current lab members: Bhuvsmiita Bhargava, Eric Carmona, Kailot Harris, Nathan Johnson, Karl Larson, Caitlin Parke, and Yueming Song. The countless hours that we have spent in discussion, collaboration, and support has been integral. You are the reason that this lab is a wonderful environment and why the group's culture is so positive. It has been a pleasure working with you.

I would also like to thank the members of Dr. Rubloff's group, specifically David Murdock, for their collaboration and Dr. Wachsman's group for the in-office discussions and use of their microscopy instrument.

Finally, I'd like to thank my family and friends. Their support has meant the world to me.

# Table of Contents

Dedication .....	ii
Acknowledgements .....	iii
Table of Contents .....	iv
List of Tables .....	vi
List of Figures .....	vii
Chapter 1: Introduction and Overview .....	1
Chapter 2: Background .....	4
2.1 Miniature Literature Review .....	4
2.1.1 Abridged History of Lithium-ion Batteries .....	4
2.1.2 Metallic Anode Materials .....	5
2.1.3 Solid-state Electrolytes with Metal Anodes .....	7
2.2 Material Properties .....	8
2.2.1 Sodium (Na) .....	8
2.2.2 Sodium $\beta''$ -Alumina (NBA) .....	9
2.3 Previous Works .....	10
2.3.1 Challenges at the Solid/Solid Interface .....	11
2.3.2 Non-Standardized Testing Methods .....	12
2.4 Electrochemical Testing Procedures .....	13
2.4.1 Electrochemical Impedance Spectroscopy .....	13
2.4.2 Chronopotentiometry and Cycling .....	13
Chapter 3: Symmetric Through-Plane Cell .....	15
3.1 Introduction .....	15
3.2 Experimental .....	15
3.2.1 Heat Treatment of Ceramic-Oxide Discs .....	15
3.2.2 Through-Plane Cell Preparation .....	16
3.2.3 Stack Pressure Application .....	18
3.2.4 Electrochemical Testing Protocol .....	19
3.3 Results and Discussion .....	20
3.3.1 Heat Treating the Sodium $\beta''$ -Alumina Disc .....	20
3.3.2 Optimized Application of Stack Pressure .....	22
3.4 Conclusions .....	27
Chapter 4: Symmetric In-Plane Cell .....	28
4.1 Introduction .....	28
4.2 Experimental .....	29
4.2.1 Sodium Deposition .....	29
4.2.2 Surface Roughness of Sodium $\beta''$ -Alumina .....	30
4.2.3 Single-Electrode Load Application .....	30
4.2.4 Electrochemical Testing Protocol .....	31
4.3 Results and Discussion .....	32
4.3.1 Optimization of Evaporated Sodium Electrodes .....	32
4.3.2 Keyence Imaging of Discs .....	33
4.3.3 Application of Pressure .....	36

4.4 Conclusions.....	39
Chapter 5: Conclusions and Recommendations .....	40
5.1 Conclusions.....	40
5.2 Recommendations for Future Work.....	41
Bibliography .....	44

## List of Tables

<b>Table 2.1.</b> Properties of Elemental Sodium Compared to Lithium .....	8
<b>Table 2.2.</b> Properties of NBA from Ionotec Specifications .....	10

## List of Figures

<b>Figure 2.1.</b> Adapted from Ref [45], the Battaglia group determined that higher temperatures are necessary for adequate treatment of the sodium beta alumina electrolyte. Hydroxide contaminants are not sufficiently driven off at temperatures below 700°C.....	12
<b>Figure 3.1.</b> Sodium with the oxidized layer partially removed to show discernible surface contamination. The left shows exposed, pristine sodium immediately after being cut with a razor blade, while the right of the image shows oxidation due to residual (<0.1 ppm) oxygen contamination in the argon environment. ....	16
<b>Figure 3.2.</b> Schematic depicting the order of materials for the through-plane cell....	17
<b>Figure 3.3.</b> Schematic of split coin cell purchased from the MTI website. The setup purchased included a nylon sleeve and stainless steel dies. The sodium cell was fit between the dies, and a load cell was attached to the top PTFE plate. ....	18
<b>Figure 3.4.</b> Image of the pressure setup with springs to maintain constant pressure.	19
<b>Figure 3.5.</b> PEIS spectrum taken with a 10 mV amplitude from 7 MHz to 100 mHz, normalized using electrode area prior to heat treatment (red) and after treatment at 850°C for 2 hours (blue). ....	21
<b>Figure 3.6.</b> (a) Cycling at 25 $\mu$ A for a 0.78 cm <sup>2</sup> electrode area under no pressure, suggesting resistance is excessive, postulated due to lack of intimate contact (b) Repeated cycling parameters for a cell with the same dimensions under external pressure. ....	23
<b>Figure 3.7.</b> Magnified plot of Figure 3.6b, showing nonzero voltage response during a rest step. The current has been included to show competence of the instrument. ...	25
<b>Figure 3.8.</b> Critical current density test adapted from the Rettenwander group under an average pressure of 0.85 MPa (a) Magnified portion of the low-current (1 to 5, 10, and 15 $\mu$ A) cycling shown in (c). (b) Magnified portion of (c) without applied current data, showing increased resistance and voltage dipping starting at 0.16 mA cm <sup>-2</sup> . (c) .....	26
<b>Figure 4.1.</b> Schematic of proposed setup and expected transport .....	28
<b>Figure 4.2.</b> (a) Sodium pad configuration at a thickness of 5 $\mu$ , prior to optimization (b) Sodium pad configuration optimized for testing conditions at a thickness of 20 $\mu$ m with a diameter of 4 mm. ....	29
<b>Figure 4.3.</b> Sampling of nine 1mm x 1mm squares on an untreated disc. ....	30
<b>Figure 4.4.</b> Image of the isolated pressure setup. More to comment .....	31
<b>Figure 4.5.</b> (a) two NBA discs immediately after sodium evaporation (b) surviving disc, minimal oxidation around the edges, salvageable (c) disc that eclipsed the surviving disc, completely oxidized and unusable (d) Figure 4.5c with increased contrast to better show the oxidized sodium pads .....	32
<b>Figure 4.6.</b> (a) SEM Image taken of an untreated sodium $\beta$ "-alumina disc with a 200 $\mu$ m scale (b) Keyence data at 5x magnification with a corresponding 500 $\mu$ m scale, peak to trough range is 8 $\mu$ m (c) 10x magnification with a corresponding 100 $\mu$ m scale (d) 20x magnification with a corresponding 50 $\mu$ m scale.....	34

**Figure 4.7.** (a) Topographic image of a 1x1 mm<sup>2</sup> sample at 20x magnification on the surface of the solid electrolyte disc (b) further analysis of large divots found (c) topmost divot from (b) with a depth of 9.231 microns (d) midrange divot from (b) with a depth of 8.860 microns (e) bottommost divot from (b) with a depth of 10.044 microns..... 35

**Figure 4.8.** Cycling data of the symmetric in-plane cell without applied load. In this test, the current density ranged from 0.04 to 0.4 μA cm<sup>-2</sup>. Current was increased stepwise in 20-minute increments with a short (2 minutes) rest step between each constant current application.. This suggests that interfacial contact between the electrode and electrolyte is sufficient. .... 36

**Figure 4.9.** Stepwise increase from 0.4 μA cm<sup>-2</sup> to 0.55 μA cm<sup>-2</sup> (red). Cell resistance increases significantly at 0.55 μA cm<sup>-2</sup>, as depicted by the voltage response (blue).. 37

**Figure 4.10.** (a) Consistent cycling at a current densities of 0.2 mA cm<sup>-2</sup> under approx. 8MPa. (b) Stepwise increase of current from 0.2 to 0.4 mA cm<sup>-2</sup>. .... 38

## Chapter 1: Introduction and Overview

Over the past century, the effects of burning fossil fuels have become devastatingly apparent, and the subsequent climate change due to released greenhouse gases is an urgent global concern. Carbon dioxide is one such heat-trapping gas. Its production has more than doubled in the past 50 years, reaching 4,857 million metric tons in 2019, and now accounts for over 75% of greenhouse gas emissions.<sup>1</sup> The majority of this stems from nonrenewable resources and industrial processes. Transportation has evolved to become the largest emitter of CO<sub>2</sub> in the US (29%), followed closely by electrical power (24%) and industry (23%). Within the transportation sector, emissions from passenger and commercial vehicles, ships, trains, and airplanes are collected. Across these, 90% of fuel sources are petroleum-based.<sup>2</sup> Already, there has been a push to electrify cars with many automakers aiming to have electric-only vehicles by the mid 2030s.<sup>3</sup>

Daily per capita residential energy consumption in the US was 12.1 kWh in 2020.<sup>4</sup> As such, there is a demand for sustainable and powerful sources. Efforts to replace petroleum, natural gas, and coal consumption, have resulted in a shift toward renewable resources such as solar or wind energy. These are promising but transient energy producers, relying on efficient storage systems to maintain the magnitude and consistency needed for consumer use. Thus, they are not yet suitable for large scale applications. Optimization of electrochemical energy storage is integral to the development of sustainable energy technologies. In fact, batteries are incredibly

versatile with applications that can range from small devices to electric vehicles and energy storage grids.

At a basic level, batteries comprise of a positive electrode, a negative electrode, and an ionically conducting electrolyte. They convert chemical energy to electrical energy through reduction and oxidation (redox) reactions at the cathode and anode, respectively. The electrolyte selectively facilitates ionic transport and prevents electronic transport, forcing electrons to flow through an external circuit that powers our devices.

Ionic salts dissolved in organic solvents are used as liquid electrolytes in commercially available lithium-ion batteries due to their high ionic conductivity. The high reactivity of metallic anodes with these organic solvents makes using these electrolytes unfeasible. The response is to employ solid-state electrolytes, which have higher chemical, thermal, and mechanical stability. Challenges with solid electrolytes are plentiful, as they similarly experience dendritic growth as well as concerns specific to the solid-solid interface, as will be described in Section 2.3.1.

In this study, we aim to analyze the effect of various applied pressures on cell cyclability and possible void formation. As mentioned, previous work from other groups has included cycling at various current densities, EIS spectra, and varying pressure within these tests. We wish to compare our results to the literature in order to verify the accuracy of our methods.

However, we have encountered a lack of reliable, standardized methods of preparation and analysis for these cells.<sup>5</sup> In broad strokes, ensuring that the solid/solid interface is not contaminated and maintaining sufficient contact throughout the test

are important, but there is no generally agreed-upon “best practice” for any step of the process. Thus, we are working to create a relatively standardized protocol for measuring EIS, cycling to critical current density, maintaining consistent pressure, and surface imaging.

## Chapter 2: Background

### 2.1 Miniature Literature Review

#### 2.1.1 Abridged History of Lithium-ion Batteries

Lithium-based batteries have been researched for over a half-century, first gaining traction after the success of the lithium-iodine battery. In the 1970s, as energy demands from the military and consumers rose, researchers explored the use of lithium metal anodes.<sup>6</sup> Intercalation compounds had not been discovered, so molten lithium anodes, were considered for a prototypical rechargeable battery. However, the molten lithium systems proved costly and corrosive, eventually being abandoned.<sup>7</sup>

1978 saw the implementation of intercalation compounds into lithium-ion batteries, and their use as cathodes allowed for the creation of the first rechargeable lithium-based battery. However, safety concerns peaked in the 1980s as operational failures and compromised cell components led to thermal runaway and explosions. Research using pure lithium metal heavily subsided, and in the 1990s, Sony commercialized a lithium-ion battery based upon two intercalating electrodes, thereby avoiding the metal anode.<sup>7</sup>

Since, lithium-ion batteries have been integrated into a multitude of gadgets, operating at a high energy density, compared to alternatives, and allowing for increased portability of devices such as computers, phones, and cameras. However, to

keep up with the increasing energy demand, current batteries require significant improvements.

### 2.1.2 Metallic Anode Materials

Elemental lithium has the most negative reduction potential (-3.04 V v. SHE) and highest specific capacity (3,860 mAh g<sup>-1</sup>). It also has a low atomic weight with the lowest density of any metal.<sup>8</sup> These properties have made it a theoretically ideal anode material for high energy batteries, but lithium metal itself is extremely reactive and hazardous. As described in Section 2.1.1, to harness the potential, but address safety concerns of a metallic anode, the lithium-ion battery was created.<sup>6</sup> However, the aforementioned increased desire for higher energy compared to current capabilities is bringing metal anodes back into light.

Batteries containing metallic anodes exhibit similar issues to those with traditional ion composite anodes, though their mechanisms may differ. Filament propagation and the subsequent short circuiting and ignition of cells are among the more dangerous issues.<sup>9</sup> Due to its extremely reactive nature, liquid organic electrolytes often decompose on the metal leading to continual capacity fade.<sup>10,11</sup> Thus, solid electrolytes have been widely investigated, ushering in a slew of new issues that were previously unconsidered. Namely, maintaining interfacial contact and conductivity of the ions between the metal and solid-state electrolyte.<sup>12</sup> Aside from this, there are other challenges faced at the solid electrode/solid electrolyte interface, such as interfacial resistance due to the formation of an unstable solid electrolyte interface (SEI), wettability of the electrode to the electrolyte, and more.<sup>13</sup> These will be addressed in Section 2.3.1. Despite challenges, pursuing a metal anode over a

composite has many advantages, specifically in high theoretical capacity and the subsequent prospect of increased energy density.

A sodium metal / Na<sup>+</sup>-conducting solid electrolyte interface has many processes and properties that are very similar to a lithium metal / Li<sup>+</sup>-conducting solid electrolyte. Sodium metal is fairly similar to lithium. It has similar mechanical properties, though is a softer metal, and both have high reactivities as alkali metals. It is also a very cost effective metal. Similarly, sodium β<sup>''</sup>-alumina (NBA) is comparable to LLZO, a common ceramic electrolyte used in lithium cells. It is also less expensive than its lithium-based counterpart, and significant research has been completed on NBA as an effective electrolyte.

Pursuing a Na metal anode has many advantages though it has a lower theoretical capacity than lithium. Sodium still has relatively high specific capacity (1167 mAh g<sup>-1</sup>) as well as significantly abundant and low cost. Using Na, however, presents alternative challenges. Na is significantly less energy-dense than Li, though resulting in a lower cell potential by about 0.3V for sodium-based cells.<sup>17</sup> Another primary issue with the use of Na metal is its propensity for dendrite formation and high reactivity. Its low melting point is also a possible safety hazard, though some researchers have taken advantage of this property, reporting good stability with molten sodium or liquid alloys.<sup>18,19</sup> Unlike Li metal, Na metal does not alloy with aluminum, allowing for the use of cost efficient current collectors when assembling a full cell. Despite best efforts, an effective commercial all solid-state battery featuring a metal anode and electrolyte is still in design.<sup>20</sup>

### 2.1.3 Solid-state Electrolytes with Metal Anodes

The general requirements for an electrolyte are as follows: thermal, chemical, and electrochemical stability, high ionic conductivity, negligible electronic conductivity, and are ideally nontoxic, sustainable, and cost-effective.<sup>22</sup> In commercial lithium-ion cells, a salt dissolved in an organic solvent is used as the liquid electrolyte. Because of the reactivity and decomposition of the electrode, liquid electrolytes are not often employed in cells featuring a metal anode. In fact, sodium metal is not compatible with the organic solvents leading to significant capacity fade. The sodium reacts with the electrolyte to form a solid electrolyte interphase (SEI) layer. Like with sodium composite electrodes, it is possible for SEIs to crack due to stress from volume changes during cycling. This compromises the passivating layer and requires further reaction between the sodium and electrolyte, consuming both, and resulting in this capacity fade.

While polymer electrolytes show stable properties and can be flexible and have a variety of applications, they are not optimal choices for energy dense solid-state batteries, as they suffer from poor ionic conductivity ( $10^{-5}$  to  $10^{-7}$  S  $\text{cm}^{-1}$ ) at room temperature. While this may be acceptable at a thin-film scale, it is not sufficient at the macroscale.<sup>21,22</sup> A majority of ionic transport occurs when the polymer is in the amorphous phase (region). However, polymer electrolytes tend to be crystalline at ambient temperature. The polymer electrolytes must therefore operate at temperatures no less than 60°C to have reasonable ionic conductivities.<sup>23,24</sup> Work has been done to increase the conductivity of these electrolytes, through cross-linking and additives.

Inorganic solid electrolytes also show possibility of enabling cells with a volumetric energy density of greater than 1 kWh/L.<sup>18</sup> Ceramic oxide electrolytes have shown to have better ionic transport than their polymer counterparts and are more chemically robust than liquid electrolytes. Solid oxide ceramics (e.g., alumina) are common due to their structure, as the alternating closely and loosely-packed layers allow for sufficient sodium transport, effectively combating the major drawback of low ionic conductivity.<sup>25-28</sup> Furthermore, alumina is a cost-effective material.<sup>25,29</sup> Solid oxide ceramics often exhibit superior electrochemical stability and are extremely thermally stable. However, they sacrifice ionic conductivity, though the beta alumina electrolyte has been found to maintain a relatively high ionic conductivity.<sup>29</sup>

## 2.2 Material Properties

### 2.2.1 Sodium (Na)

As described in Section 2.1.2, sodium metal has a low redox potential (-2.71 V vs. SHE) and high theoretical capacity of 1167 mAh g<sup>-1</sup>, making it an appealing anode material. Table 2.1 compares lithium and sodium. Though no metal is as energy dense as lithium, the abundance of sodium is significant, showing promise of a more sustainable material.

**Table 2.1.** Properties of Elemental Sodium Compared to Lithium

Element	Sodium (Na)	Lithium (Li)
Atomic Weight (g)	22.9898	6.941

Abundance (% of Earth's crust)	2.3	0.003
Melting Point (°C)	97.81	180.5
Density (g/mL)	0.971 (at 20°C)	0.534 (at 20°C)
Oxidation States	+1, -1 (rare)	+1
Ionic (+1) Radius (pm)	116	90
Potential (V vs SHE)	-2.71	-3.04
Theoretical Capacity (mAh g <sup>-1</sup> )	1167	3860

Both sodium and lithium are soft metals with a low yield strength; thus, they deform readily under pressure. Sodium is, however, significantly softer and therefore creeps significantly faster than lithium.<sup>30</sup> While Na and Li are not exactly analogous, it is possible to gain insights about lithium from sodium.<sup>31–33</sup> Additionally, sodium has a larger atomic radius and mass than lithium, which affects ionic conductivity and its concentration in a solid electrolyte.<sup>34</sup>

Despite its high reactivity, sodium does not alloy with aluminum like lithium does. This enables use of aluminum current collectors in full cell assemblies. Copper, the current collector material traditionally used in lithium-ion batteries, is both heavier and more expensive.<sup>34</sup> Thus, incorporating sodium metal allows for a cheaper overall cost. It should be noted that employing high-cost materials in electrode composites and electrolytes discredits the cost effectiveness of sodium.

### 2.2.2 Sodium $\beta''$ -Alumina (NBA)

Beta alumina electrolytes have been researched extensively since the mid-20<sup>th</sup> century in conjunction with a variety of ions including, but not limited to, Na<sup>+</sup>, K<sup>+</sup>, and Li<sup>+</sup>. The material used in this study is polycrystalline sodium  $\beta''$ -alumina (Na<sub>2</sub>O•5Al<sub>2</sub>O<sub>3</sub>).<sup>35</sup>

**Table 2.2.** Properties of NBA from Ionotec Specifications

Crystallinity	Polycrystalline
Phase Content (% $\beta''$ -alumina)	90-95
Porosity (%)	1-2
Maximum Pore Size ( $\mu\text{m}$ )	5-20
Ionic Conductivity ( $\text{S cm}^{-1}$ )	0.002
Thermal Expansion Coefficient ( $\times 10^{-4} \text{ }^\circ\text{C}$ )	7.2 (0-500 $^\circ\text{C}$ ) 8.6 (500-1000 $^\circ\text{C}$ )
Fracture Toughness ( $\text{MPa m}^{1/2}$ )	2-3
Bending Strength (MPa)	250-300
Thermal Stability ( $^\circ\text{C}$ )	1000
Disc Thickness (mm)	1.0

The purchased NBA discs have an area-specific ionic resistance (ASR) of 60  $\Omega\text{cm}^2$ . This was determined by using the equation:  $\text{ASR} = \frac{L}{\kappa}$  where L is the thickness of the electrolyte and  $\kappa$  is the ionic conductivity of the electrolyte. Ionic conductivity as well as all data in Table 2.2 were obtained from the specifications on the Ionotec website.<sup>36</sup> This electrolyte is mechanically strong, making it resistant to volumetric changes upon stripping and plating, and its high conductivity compared to other inorganic solid oxide electrolytes is very attractive to researchers.<sup>26,37,38</sup>

### 2.3 Previous Works

Previous work has been done by various groups to investigate the effects of pressure on the solid electrolyte-electrode interface. Research by the Sakamoto and Bruce groups have been of particular interest to us.

### 2.3.1 Challenges at the Solid/Solid Interface

Prominent efforts are being made to better understand the metal anode/solid electrolyte interface, and various groups have observed an increased resistance prior to a short circuit during cycling. It is generally understood that a high current density can lead to short circuiting, but the details of this mechanism are not well understood. The Sakamoto group has theorized that a critical current density (CCD) must be reached before short circuiting can occur. CCD is defined as the maximum sustainable current density without short-circuiting as a function of temperature.<sup>39</sup> For this reason, CCD plays an important role in filament formation, as localized CCD can differ from the bulk CCD, leading to uneven plating and dendritic growth.<sup>31</sup>

Furthermore, the Bruce group investigates a phenomenon observed in cells with both lithium and sodium metal anodes and solid electrolytes.<sup>40,41</sup> Voids formed at a current density “above which Li is stripped faster than it is replenished at the Li/SE interface”.<sup>31</sup> Visually, they are areas at which the metal anode and solid electrolyte do not make contact, resulting in a significantly decreased active area. This could allow for the CCD to be reached locally despite a low bulk current density. Kasemchainan, et al. postulates this high CCD can result in void formation, leading to uneven plating and filament propagation, eventually leading to a short circuit.<sup>31</sup> Voids can be even found on pristine interfaces and increase upon stripping the metal. Plating, however, does not fill the voids to their previously uncycled states, and this asymmetry leads to an accumulation of void space over time and cycles.<sup>40</sup> Multiple groups have explored this phenomenon and postulated that applying an external or stack pressure can inhibit the void formation.<sup>40,42,43</sup>

Wettability onto the electrolyte is also a concern with metal electrodes, as poor wettability decreases interfacial contact. While extensive research has been done on lithium metal,<sup>39</sup> sodium metal has not found such success. Progress has been found through using liquid or molten metal, or by alloying the sodium with Cs, K, or other elements.<sup>18</sup>

### 2.3.2 Non-Standardized Testing Methods

Upon further examination of the literature, it is clear that a lack of consistent methods can be found from group to group. An example of this is in the pretesting treatment of electrolyte discs. Previous work by the Battaglia group shows that for the NBA electrolyte, heat treatment at 400°C is not sufficiently high to drive off contaminating species. They explore the effect of various temperatures, determining an optimal treatment temperature of 900°C.<sup>44</sup>

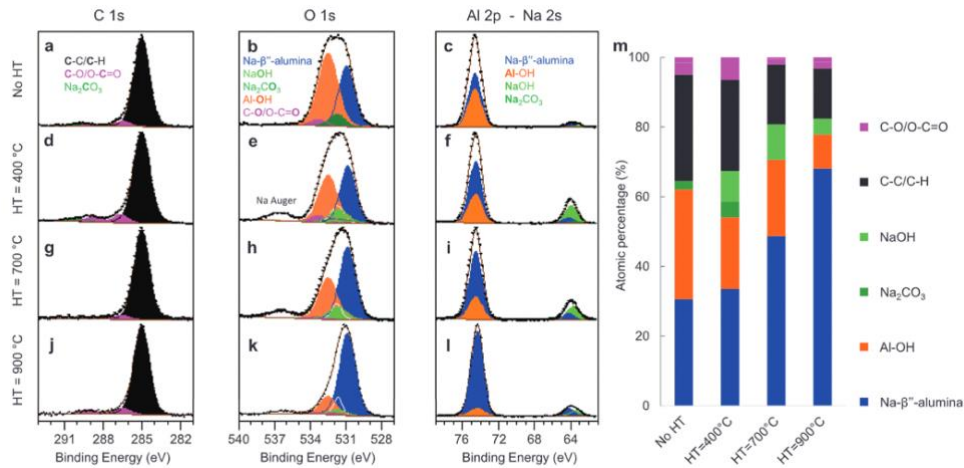


**Figure 2.1.** Adapted from Ref [45], the Battaglia group determined that higher temperatures are necessary for adequate treatment of the sodium beta alumina electrolyte. Hydroxide contaminants are not sufficiently driven off at temperatures below 700°C.

This treatment cannot be well compared to the electrolyte treatment from the Sakamoto group, as they used synthesized LLZO and performed their treatment at

400°C for 12 hours.<sup>39</sup> However, the Bruce group follows the electrolyte treatment method of the Sakamoto group for both their LLZO and NBA samples.<sup>11,12,36</sup>

## 2.4 Electrochemical Testing Procedures

### 2.4.1 Electrochemical Impedance Spectroscopy

Potentiostatic Electrochemical Impedance Spectroscopy (PEIS) and Galvanostatic Electrochemical Impedance Spectroscopy (GEIS) are methods used to determine the resistance within a cell. It works by varying the potential and recording the current, or varying the current and recording the potential. It is possible to use a spectrum to differentiate the contributions of various sources of resistance by employing an equivalent circuit model, including electrolyte structure. Further insight into effects of grain boundaries and other electrolyte properties is beyond the scope of this study.

PEIS was selected over GEIS as previous works featuring impedance data have employed PEIS, allowing for data to be more easily compared. Rarely, GEIS has been used in the literature, though both methods are appropriate and give equivalent results. It is important to note that electrochemical impedance spectroscopy is only valid across domains of constant potential or current. Thus, data generated from a transient system can contain artifacts.

### 2.4.2 Chronopotentiometry and Cycling

Chronopotentiometry is a relatively simple technique, as it regards applying a constant current and measuring the resulting voltage response. It is useful in the larger scheme of cell cycling and galvanostatic intermittent titration technique (GITT, which

may also be abbreviated to GCPL from EC-Lab software). To cycle a cell, electrode capacity and areas are calculated to find appropriate current densities using the equation  $m = \frac{M I t}{n F}$ . In this, m is the mass (g) of the electrode (determined through a volume/density conversion), I is the applied current in A, t is the time in seconds, n represents the equivalents of electrons (1 mol e<sup>-</sup> for our purposes), and F is Faraday's constant.

## Chapter 3: Symmetric Through-Plane Cell

### 3.1 Introduction

Sodium metal anodes have attracted increasing attention due to their high attainable energy density. However, as with all metallic electrodes, they pose significant challenges in stability and longevity. One method to explore this includes employing symmetric cells. Though these cells have 0 voltage and are not useful for practical applications, they can provide important insights into the material interactions. Specifically, we can use a symmetric cell to better understand the fundamental mechanisms at the solid-solid interface<sup>46</sup> and potential failure pathways that arise from issues at the interface.<sup>47</sup> Symmetric cells have been used by various other groups for analysis of filament formation and pressure effects.<sup>20,48-50</sup> The goal of the symmetric through-plane cell is to better understand the effects of disc treatment interactions between the metal anode and solid electrolyte.

### 3.2 Experimental

#### 3.2.1 Heat Treatment of Ceramic-Oxide Discs

Polycrystalline Sodium  $\beta''$ -Alumina ( $\text{Na}_2\text{O} \cdot 5\text{Al}_2\text{O}_3$ ), discs of 1.0 mm thick and 20 mm diameter were purchased from Ionotec Ltd. Prior to use, the surfaces of NBA discs were sputtered with gold and analyzed using SEM in accordance with the literature and will be further discussed in Section 4.3.2. After observing the surface under 100x, 500x, and 1000x magnifications, it was decided that further polishing

was not necessary. Heat treatment was pursued due to high impedance attributed to species at the electrolyte surface. To heat treat, the discs were placed in an alumina crucible. The treatment was done in an 1100°C muffle furnace purchased from MTI. To prevent cracking the ceramic, the heating procedure employed a 4°C per minute ramp rate from 25°C to 850°C. The temperature was held at 850°C for 2 h to ensure oxidized species and carbonates were driven off, and the furnace and contents were allowed to cool to room temperature (23°C). Heat treatment was performed in an Ar-filled glovebox.

### 3.2.2 Through-Plane Cell Preparation

A sodium metal ingot was obtained from United Nuclear packaged under argon. The oxidized outer layers were removed using a razor blade, and unreacted sodium was obtained. Figure 1 shows visible contrast between pristine and oxidized sodium.

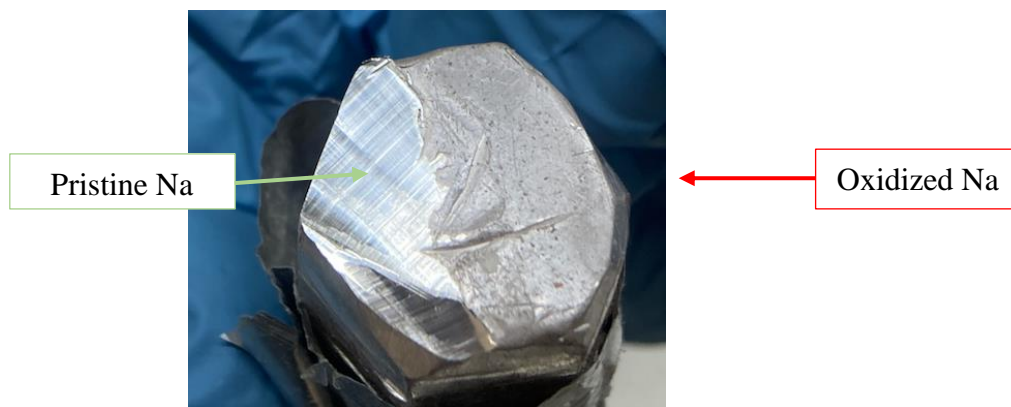


**Figure 3.1.** Sodium with the oxidized layer partially removed to show discernible surface contamination. The left shows exposed, pristine sodium immediately after being cut with a razor blade, while the right of the image shows oxidation due to residual (<0.1 ppm) oxygen contamination in the argon environment.

The sodium was cold rolled to a foil with a thickness of approximately 500  $\mu\text{m}$ , and electrodes were punched using an 8 mm manual punch. The electrodes were mechanically cleaned with a nylon brush, aligned, and applied to a heat-treated NBA disc. The electrode sides that were exposed to the glovebox environment were covered with aluminum foil (Reynolds Wrap of approximately 20  $\mu\text{m}$  thickness) and cut to an appropriate diameter. The aluminum foil was sized slightly larger than the electrodes to allow for deformation of the electrodes under pressure. Light pressure ( $<1$  MPa) was applied to both sides of the cell to ensure contact between the foil, electrodes, and electrolyte before the cell was placed into the sleeve.

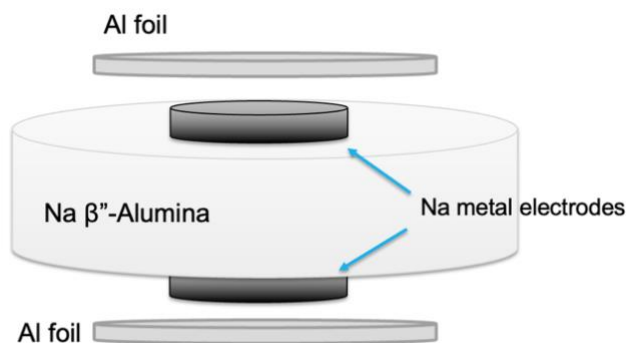


**Figure 3.2.** Schematic depicting the order of materials for the through-plane cell.

The symmetric cell was then placed in a split coin cell shown in Figure 3.2. The split cell used to align the components for testing was obtained from MTI (#EQ-PSC). This setup includes two stainless steel die, a nylon sleeve, PTFE caps, and compression nut. The sleeve has a 25 mm inner diameter. Caps were secured to the dies to avoid alignment inconsistencies during testing. Cell preparation was performed in an Ar-filled glovebox.

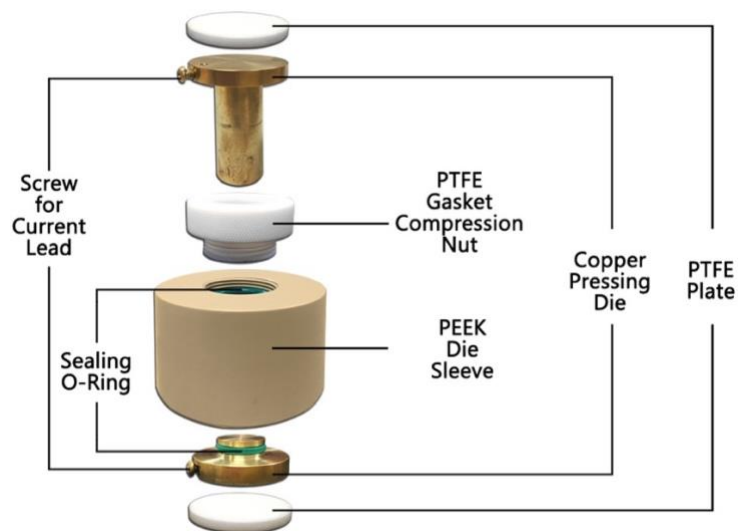


**Figure 3.3.** Schematic of split coin cell purchased from the MTI website. The setup purchased included a nylon sleeve and stainless steel dies. The sodium cell was fit between the dies, and a load cell was attached to the top PTFE plate.

### 3.2.3 Stack Pressure Application

A screw-type jig (EQ-JIG-1) was purchased from MTI and used to apply external stack pressure on the dies. The jig was outfitted with springs to maintain a constant pressure. A 1 kN load cell (9C9-1KN) from HBK was used with ClipX and DataView software to measure the applied force. This was converted to MPa based on the approximate area of the sodium electrodes. The load cell was affixed to one PTFE cap and die to ensure alignment between the sensor, cell, and jig.

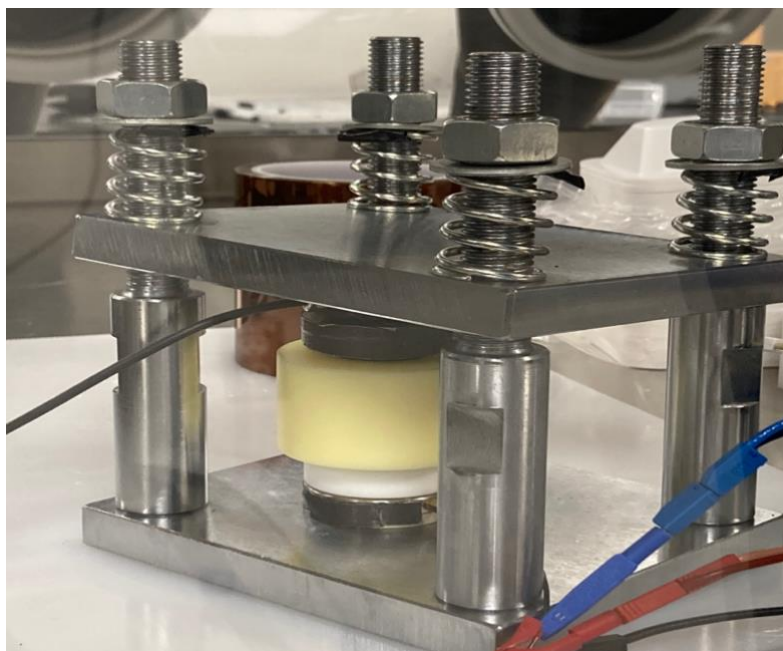


**Figure 3.4.** Image of the pressure setup with springs to maintain constant pressure. Not pictured: Leveling tool used to maintain a flat upper plate

Once the cell was assembled, a force of 100N was applied to allow for the initial deformation of the electrodes. After 1.5 h, the cell was removed from the setup. The area of each electrode was measured, and force was adjusted to give an applied pressure of 1 MPa. An electrode diameter of 8 mm was chosen, as after deformation, it is reached approximately 10.5 mm in diameter (to get 100 mm<sup>2</sup> active area).

#### 3.2.4 Electrochemical Testing Protocol

Potentiostatic electrochemical impedance spectroscopy was done to determine general impedances in the cell. Drawing from the literature an amplitude of 10 mV was used for the technique and the frequency was varied from 7 MHz to 500 mHz. A frequency range from 7MHz to 100 mHz was used with fewer points per decade in the event of an insufficient spectrum. To maintain pseudo-steady state, the PEIS scans were kept to under one minute.

Cycling procedures were similarly collected from the literature. The initial testing protocol we used looked at increasing current density stepwise. The protocols for later critical current density testing were adapted from Rettenwander<sup>51</sup> and adjusted for the active electrode area. Electrochemical measurements were taken using a Biologic SP-300 and its corresponding EC-Lab v11.36 software. All testing was performed at room temperature (23°C).

### 3.3 Results and Discussion

#### 3.3.1 Heat Treating the Sodium $\beta''$ -Alumina Disc

Prior research on disc treatment has been done by various groups who synthesized sodium  $\beta''$ -alumina. However, we looked at whether it was necessary to heat treat after factory-preparation. Jolly, et al.<sup>11</sup> performed heat treatment at 400°C for 12 hours on discs also purchased by Ionotec. However, Bay, et al.<sup>35</sup> heat-treated synthesized discs at 900°C for 3 hours. We concur that heat treatment is a crucial pretesting step that affects interfacial resistance. However, heating for 12 hours is not necessary. If a higher temperature is used, the duration of heat treatment can be decreased. In fact, this is preferred due to contaminating species (e.g., Al-OH) desorbing at higher temperatures. Figure 3.5 shows an impedance spectrum prior to (red) and after (blue) heat-treatment. Electrodes were prepared as described in Section 3.3.2 and had an area of 0.78 cm<sup>2</sup>.

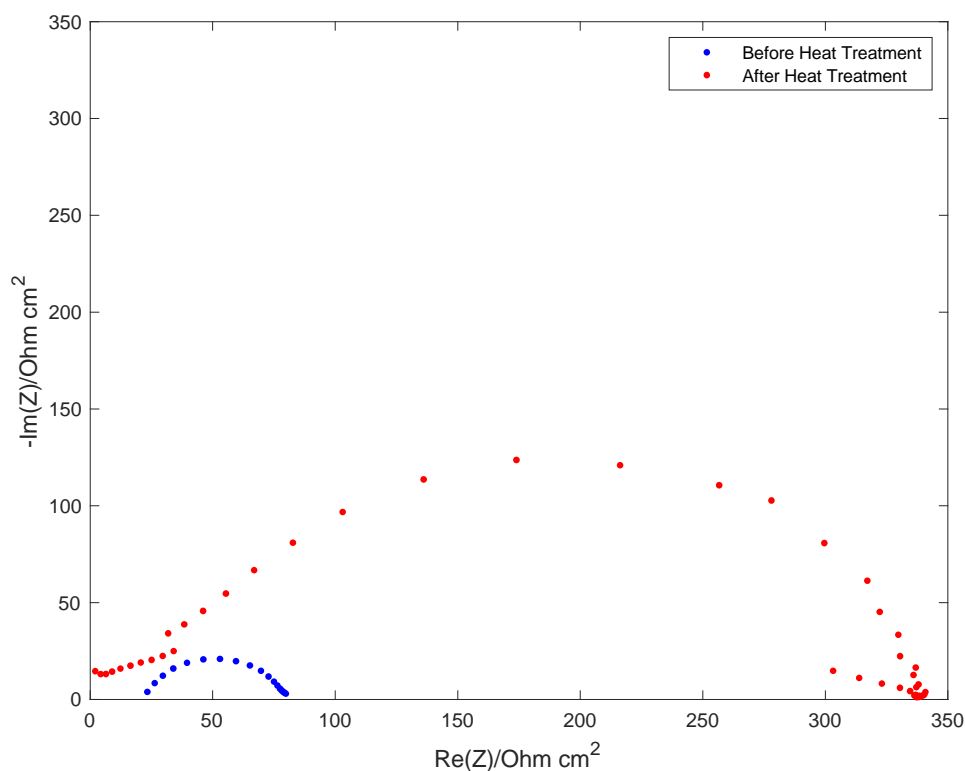


**Figure 3.5.** PEIS spectrum taken with a 10 mV amplitude from 7 MHz to 100 mHz, normalized using electrode area prior to heat treatment (red) and after treatment at 850°C for 2 hours (blue).

The spectra were normalized using the active electrode area. It is evident that interfacial resistance has been reduced, though polishing was part of the commercial disc treatment process at the manufacturer Ionotec. The PEIS from the untreated disc features a slight dovetail in the low-frequency region. This can be attributed to either surface contaminants, such as adsorbed species, or transience during the PEIS scan. As mentioned in Section 2.4.1, an accurate EIS spectrum must be taken during steady state, or at least pseudo-steady-state conditions. Analysis considering the effects of grain boundaries on the surface impedance is beyond the scope of this thesis.

### 3.3.2 Optimized Application of Stack Pressure

Upon initial cycling of the through-plane symmetric sodium cell, it was immediately apparent that pressure was necessary for any sort of reliable voltage response. As a preliminary test, we attempted to perform chronopotentiometry on the cell. The current was set to 25  $\mu\text{A}$  for 10 mm diameter sodium electrodes (current density of  $0.03 \frac{\text{mA}}{\text{cm}^2}$ ) under no pressure. This current density was chosen, as Jolly, et al.<sup>40</sup> found that cells without external pressure were able to cycle reliably at  $0.25 \frac{\text{mA}}{\text{cm}^2}$ , failing at  $0.5 \frac{\text{mA}}{\text{cm}^2}$ . This suggested that our initial cell would cycle dependably. The resulting plot of potential versus time (Figure 3.6a) shows high resistance within the first 20 seconds, and the test ended after two minutes. The voltage response ( $>10\text{V}$ ) is attributed to excessive resistance, as the Biologic instrument applied an accurate current. Further, verification of the instrument using the calibration materials and our own MTI cell was done prior to and after this experiment, suggesting the issue was not with the Biologic SP-300.

This enormous resistance is due to a lack of intimate interfacial contact between the electrodes and the electrolyte. While it was not possible to ascertain the exact cause of this resistance, it was postulated that either interfacial chemistries (e.g., oxidation of sodium), impurities on the electrolyte surface, or insufficient stack pressure could play a large role in this lack of intimate contact.

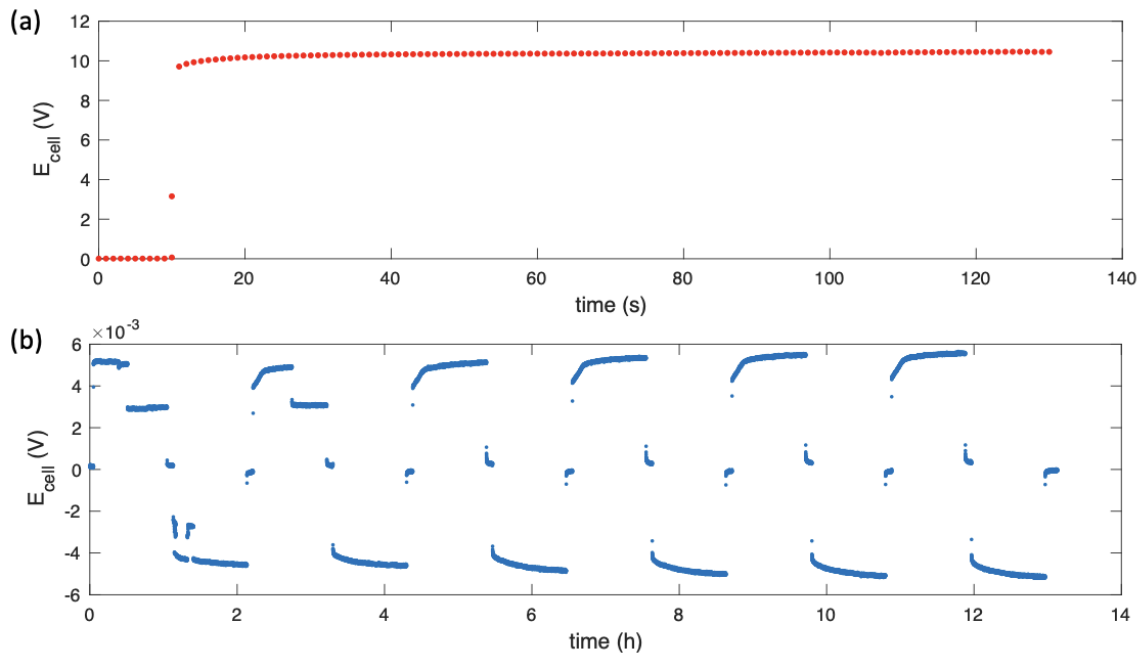


**Figure 3.6.** (a) Cycling at 25  $\mu\text{A}$  for a 0.78  $\text{cm}^2$  electrode area under no pressure, suggesting resistance is excessive, postulated due to lack of intimate contact (b) Repeated cycling parameters for a cell with the same dimensions under external pressure.

To address this, pressure was applied to the cell. After fitting the cell into the pressure jig and applying ( $>1$  MPa), the cell stably cycled at 25  $\mu\text{A}$  ( $0.03 \frac{\text{mA}}{\text{cm}^2}$ ) for over 12 hours, as shown in Figure 3.6b. Through the data, it is evident that the application of external pressure has increased contact at the electrolyte/sodium interface allowing for better cyclability.

Further observations from initial testing (Figure 3.6b) include the inconsistent voltage response within the first two cycles and the nonzero voltage during the rest step. Early-cycle voltage could be attributed to an unclean surface. Though pressure helped increase contact at the surface, oxidation of the sodium and various interfacial chemistries can also heavily affect the voltage response. As sodium is cycled, clean sodium is plated at interface, possibly leading to lower resistance. This phenomenon

would affect only the first few cycles. However, without a method relevant to understanding the intricacies of the surface chemistry, it is not possible to exactly determine the interfacial interactions.

The small but nonzero voltage during the rest step is notable, as we initially assume that both interfaces are Na metal / NBA, and therefore the open-circuit voltage should be zero. Figure 3.7 is a magnified plot from Figure 3.6b, which was done to emphasize the zero current. Despite this, there is a nonzero voltage response which corresponds to the open circuit voltage. It is nonzero likely due to surface contamination and oxidation of the sodium electrodes and NBA electrolyte. This can be contrasted with the cycling data found in Section 4.3.2. The voltage response during rest step when cycling the evaporated lateral cell does not have this relaxation pattern. A subsequent concern is that the voltage relaxation increases as the cycles increase. As shown in Figure 3.6b, there was a stepwise increase of current density, and the increasing voltage relaxation corresponds to this.

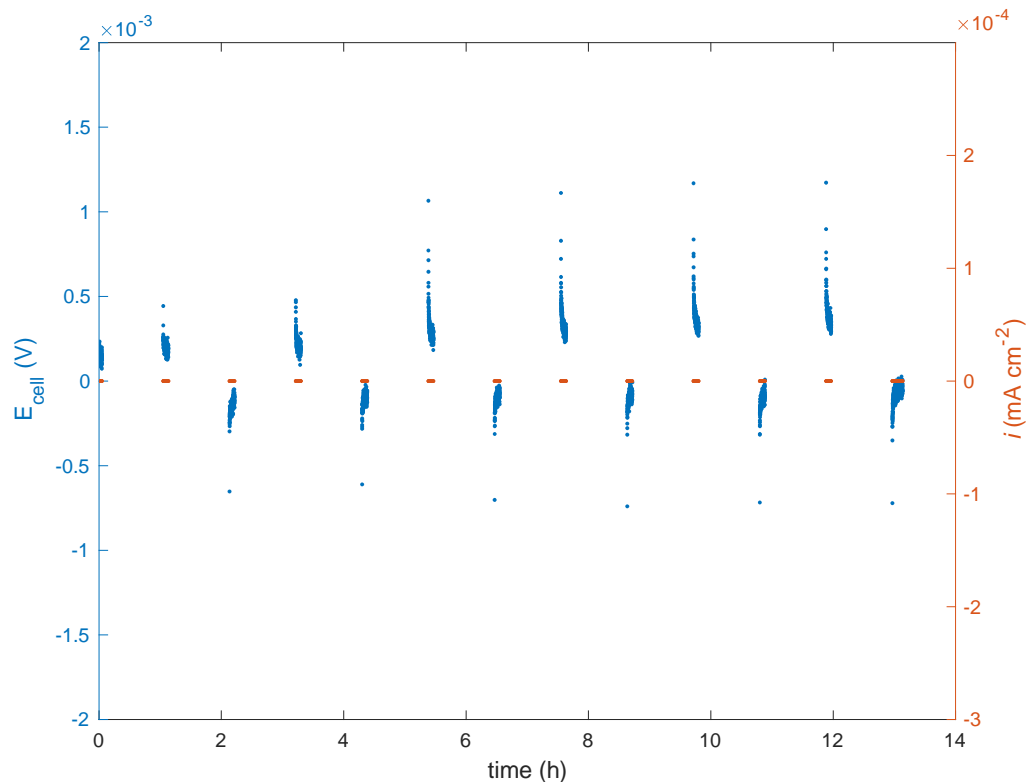


**Figure 3.7.** Magnified plot of Figure 3.6b, showing nonzero voltage response during a rest step. The current has been included to show competence of the instrument.

As pressure was applied, however, the sodium electrodes began to plastically deform. While this was not unexpected, it affected both the active electrode area as well as the applied load. We observed that applying a 100N to a cell resulted in relaxation to approximately 80N within 1 hour and further decreased to 60N within 3 hours. This introduced significant uncertainty into the testing procedure. To address this, springs were added to the jig setup as shown in Section 3.2.3 to maintain constant force on the electrodes. After adding the springs, the applied force was constant ( $\pm 3\%$ ) across 16 hours. As such, cycling was performed for the cell under constant pressure, shown in Figure 3.8.

Overall voltage and current density versus time plots are reported in Figure 3.8a. The current density ranges from 0.001 mA cm<sup>-2</sup> to 0.4 mA cm<sup>-2</sup>. At low current (e.g., <0.03 mA cm<sup>-2</sup>), significant noise is seen as in Figure 3.8b. This is likely due to the poor resolution, as this noisy behavior corresponds to 0.0001 mA cm<sup>-2</sup>. The voltage range was defined with respect to the 0.4  $\frac{\text{mA}}{\text{cm}^2}$  sequence resulting in unsuitable resolution for lower voltage responses. Thus, early cycling data contains justifiable noise.

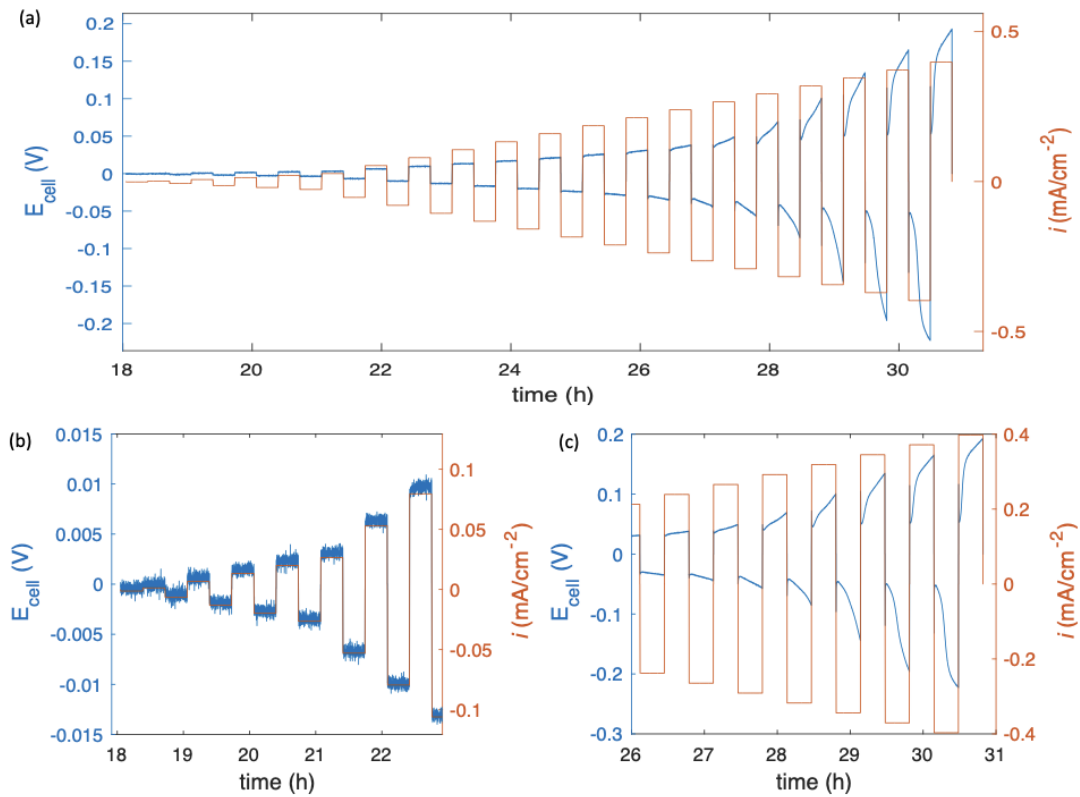


**Figure 3.8.** (a) Cell voltage and current density versus time data from the critical current density test adapted from the Rettenwender group<sup>51</sup> under an average pressure of 0.85 MPa; (b) Magnified portion of the low-current (0.001 to 0.005, 0.010, and 0.015 mA cm<sup>-2</sup>) cycling shown in (a); (c) Magnified portion of (a) without applied current data, showing increased resistance and voltage dipping starting at 0.16 mA cm<sup>-2</sup>.

In Figure 3.8c, it is evident that the resistance is increasing, but at  $0.16 \text{ mA cm}^{-2}$ , the voltage begins to dip. We find this behavior interesting, as it suggests an initial phenomenon is occurring at the interface to decrease resistance. However, this is short-lived, as the resistance increases steeply immediately after. We also observe asymmetric behavior at larger current densities ( $>0.3 \text{ mA cm}^{-2}$ ). While works have observed decreased resistance as a sign of potential short circuiting, the successive increase in resistance does not suggest this is what is occurring, and this does not explain the asymmetric voltage response. Consideration to current density and cycled sodium thickness ( $0.16 \text{ mA cm}^{-2}$  and  $\sim 4$  microns respectively) must be taken, as these are fairly low parameters for such a response. However, exact understanding of the increased resistance is not known.

### 3.4 Conclusions

The application of pressure is a necessity for cell cyclability with a through-plane symmetric cell setup. The exact value of pressure needed, however, is not explicitly known. Cyclability was achieved at 1 MPa at low current densities. It should be noted that larger current densities may require a higher applied load. However, that is out of the scope of this study. It is, however, addressed by the Sakamoto<sup>43</sup> and Bruce<sup>40</sup> groups. Other sources of interfacial resistance should be considered, as addressed in Sharafi, et al.<sup>39</sup> Significant work must be done to improve reliability of the current cell setup.

## Chapter 4: Symmetric In-Plane Cell

### 4.1 Introduction

As discussed, sodium can quickly oxidize despite minimal ( $< 0.1$  ppm) oxygen contamination in the inert atmosphere. Thus, alternative methods to apply sodium onto the heat-treated electrolyte were explored, namely via sodium evaporation. Motivation for this assumed that part of the interfacial impedance was due to oxidized sodium, skewing results. Furthermore, the in-plane cell setup shown in Figure 4.1 allows for alternative pressure tests. Investigating the effect of pressure on one electrode is not possible with the through-plane cell configuration. Employing a platen with a 4.3 mm tip was used to address this.

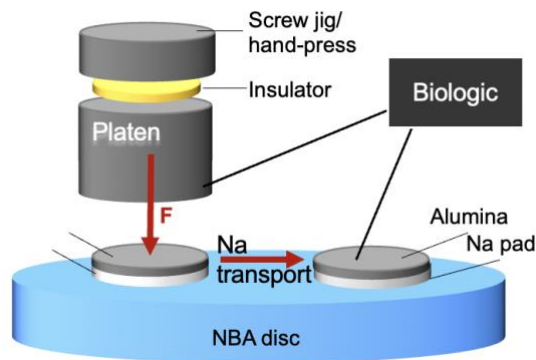


**Figure 4.1.** Schematic of proposed setup and expected transport

Previous research on thin film sodium electrodes is scarce. As such, our novel approach can explore sodium transport under stress as shown in Figure 4.1. While not

exactly comparable to the through-plane setup, the in-plane cell can provide interesting insight to mechanical effects on the electrochemical response.

## 4.2 Experimental

### 4.2.1 Sodium Deposition

Sodium  $\beta''$ -Alumina discs were heat-treated as described in Section 3.2.1 before being transported under vacuum to an evaporator. Before sodium evaporation, discs were placed in a stainless steel vessel and a corresponding mask was fitted to define sodium pad dimensions. Sodium cubes stored in mineral oil were used, and the oil was mechanically removed using a scalpel before evaporation. A shield was used to prevent evaporated contaminants from reaching the discs. The initial deposited pads were 4 mm x 2 mm x 5  $\mu$ m rectangles. Optimized pads were 4 mm diameter circles at approximately 20  $\mu$ m thick.

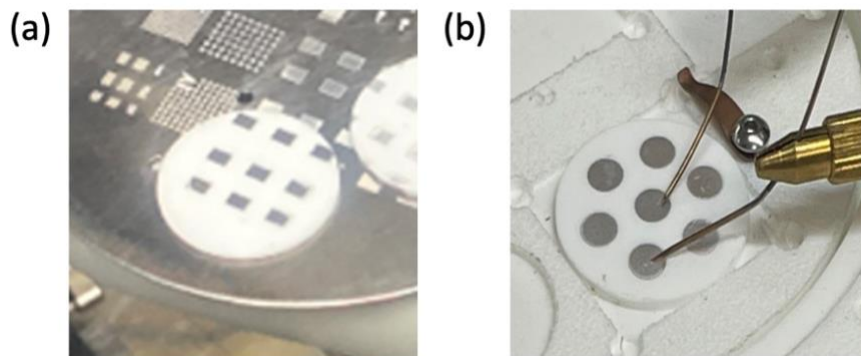


**Figure 4.2.** (a) Sodium pad configuration at a thickness of 5  $\mu$ , prior to optimization (b) Sodium pad configuration optimized for testing conditions at a thickness of 20  $\mu$ m with a diameter of 4 mm.

The pads were then coated with a thin layer ( $\leq 20$  nm) of alumina to prevent reaction with the environment. Each round pad has an active area of 0.125 cm<sup>2</sup> and a capacity

of 0.28 mAh. Micromanipulators purchased from Quater Research were connected to the Biologic SP-300, and beryllium copper probes were used for the thin-film in-plane cells.

#### 4.2.2 Surface Roughness of Sodium $\beta''$ -Alumina

An untreated disc was removed from the glovebox and transported to a Keyence VK-X3000. PTFE-tipped forceps were used to handle the disc to prevent scratching, and it was placed on a silicon-covered stage. Imaging of the disc was done at 5x, 10x, and 20x magnifications. Due to constraints of time and file size, for the 20x images, a sampling of nine 1mm x 1mm squares was performed, shown in Figure 4.3. Imaging was performed on both sides of the disc. Images were analyzed using the Keyence software.

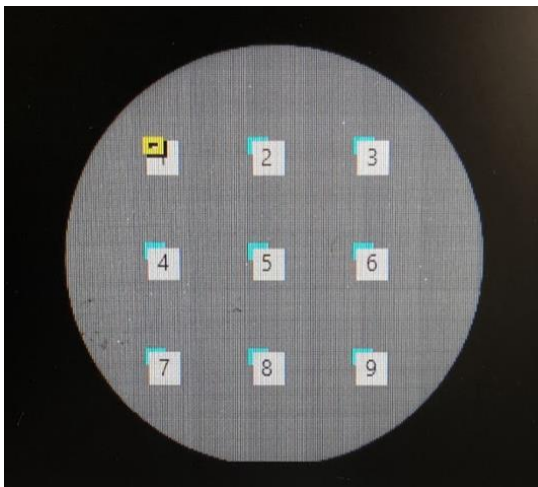


**Figure 4.3.** Sampling of nine 1mm x 1mm squares on an untreated disc.

This sampling is representative of the disc surface.

#### 4.2.3 Single-Electrode Load Application

A stainless-steel platen with a flat tip diameter of 4.3 mm was attached to a screw jig purchased from MTI (EQ-JIG-3). The sodium pad diameters were chosen to

be just smaller than the platen. Discs were placed beneath the platen, and one pad was aligned to apply uniaxial load. In this setup, pressure was applied to only one electrode, and the jig was tightened. The asymmetric load was chosen to observe the electrochemical response due to force, as explained in Section 4.1.

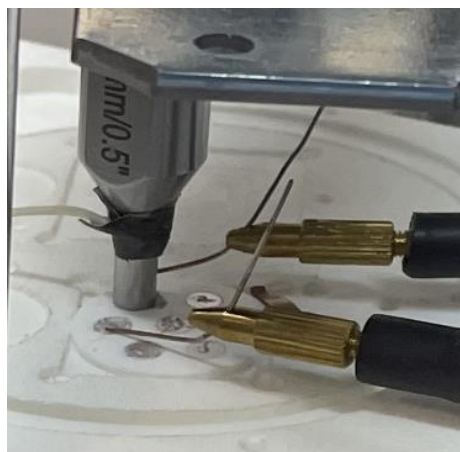


**Figure 4.4.** Image of the isolated pressure setup. More to comment

As shown in Figure 4.4, the micromanipulators were arranged such that one probe punctured the unstressed sodium pad, while the second maintained contact with the platen, and the platen was used as the probe.

#### 4.2.4 Electrochemical Testing Protocol

For the in-plane cell, testing protocols were similar to those described in 3.2.5, but scaled down for a thin electrode with small area. Current densities ranged from 0.04 to 0.55 mA cm<sup>-2</sup>. A stepwise increase of current density was pursued until cell failure. Exact values of current density and pressure will be discussed in conjunction with the results. PEIS was executed with the same parameters as described in 3.2.5. All testing was performed at room temperature (23°C).

### 4.3 Results and Discussion

#### 4.3.1 Optimization of Evaporated Sodium Electrodes

Initially, sodium was deposited onto two separate NBA discs as electrodes of 5 microns thick and 8 mm<sup>2</sup> area. However, upon transport from the evaporation chamber to the glovebox, one disc was ruined. As shown in Figure 4.5c, the deposited sodium pads fully oxidized. When agitated with forceps, the disc did not reveal sodium underneath the oxide layer. Thus, it was completely unusable.

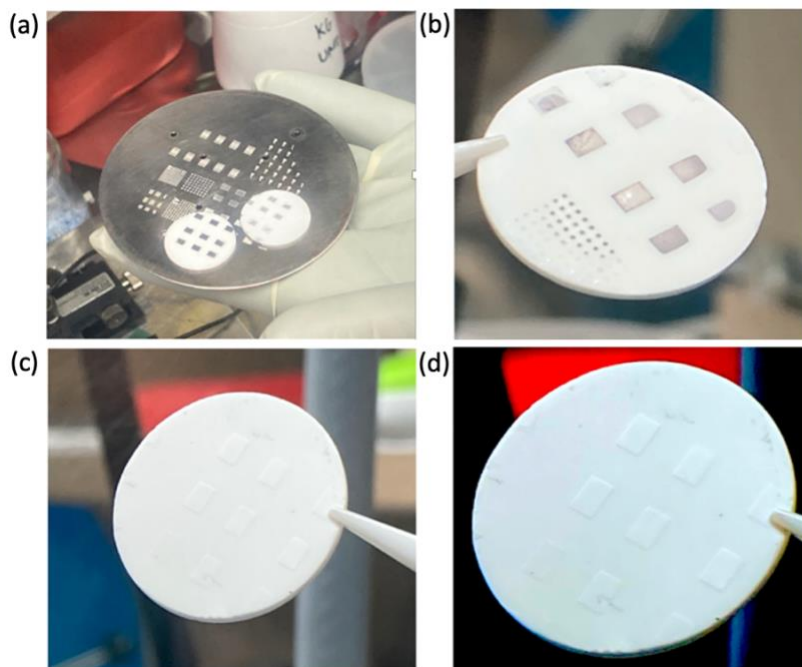


**Figure 4.5.** (a) two NBA discs immediately after sodium evaporation (b) surviving disc, minimal oxidation around the edges, salvageable (c) disc that eclipsed the surviving disc, completely oxidized and unusable (d) Figure 4.5c with increased contrast to better show the oxidized sodium pads

The disc shown in Figure 4.5b was not as affected, as it was eclipsed by the first disc. Though this disc did not show complete oxidation, the thinness of the electrodes brought issues with the micromanipulators. It was not possible to obtain

results from these pads, likely due to the micromanipulators puncturing all the way through the electrodes to the electrolyte surface.

This prompted two major questions: Is a five-micron electrode too thin for our applications? Would it be possible to protect the sodium from oxidation upon transport from the evaporation chamber to the glovebox?

#### 4.3.2 Keyence Imaging of Discs

SEM imaging had been done prior but showed a smooth enough surface for ingot testing. It was qualitatively determined that polishing further than manufacturing standards was not necessary (Figure 4.6a). However, imaging the untreated sodium  $\beta''$ -alumina disc at 5x magnification using a laser confocal microscope allowed for a quantitative analysis. The Keyence revealed that the commercial NBA discs feature striations and unevenness (Figure 4.6b) left over from the manufacturing process.

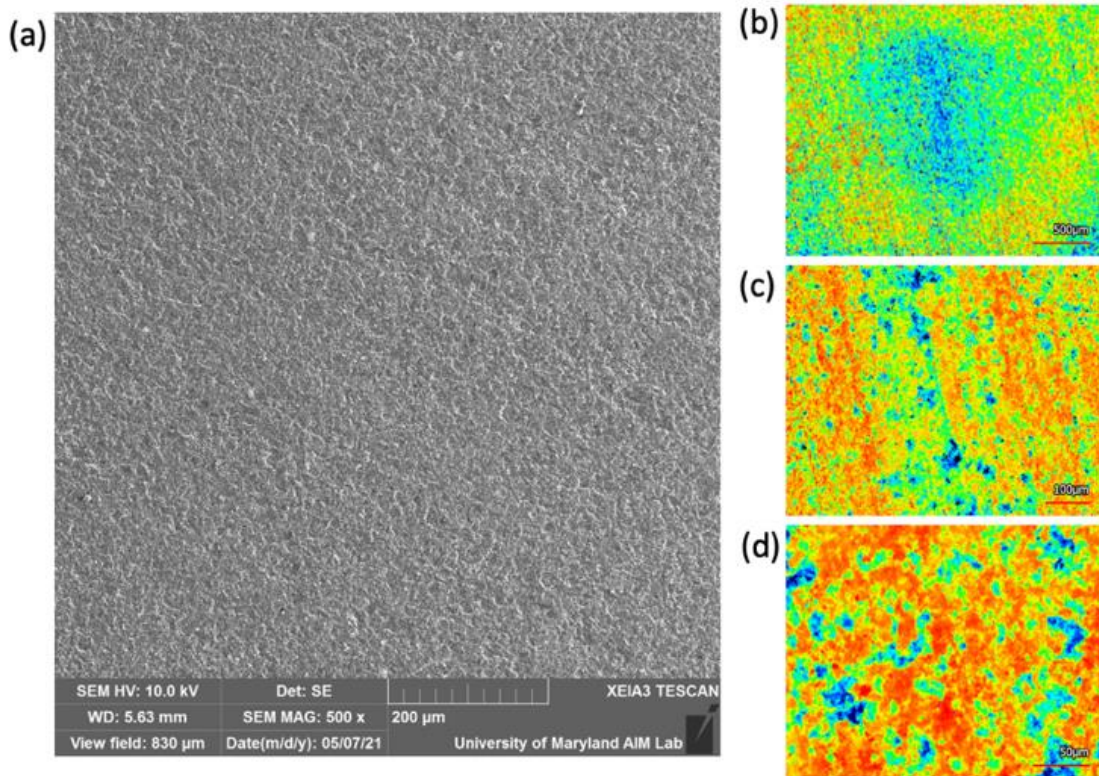


**Figure 4.6.** (a) SEM Image taken of an untreated sodium  $\beta''$ -alumina disc with a 200  $\mu\text{m}$  scale (b) Keyence data at 5x magnification with a corresponding 500  $\mu\text{m}$  scale, peak to trough range is 8  $\mu\text{m}$  (c) 10x magnification with a corresponding 100  $\mu\text{m}$  scale (d) 20x magnification with a corresponding 50  $\mu\text{m}$  scale.

The topographic maps (Figure 4.6 b-d) show roughness that was not observed on the SEM images. The scale of this roughness is large ( $>1$  micron) compared to the thickness of the sodium electrodes. At various samplings, the peak-to-trough roughness greater than 5 microns. Figure 4.7 shows an analysis of pits found on the surface from one sampling at 20x magnification.

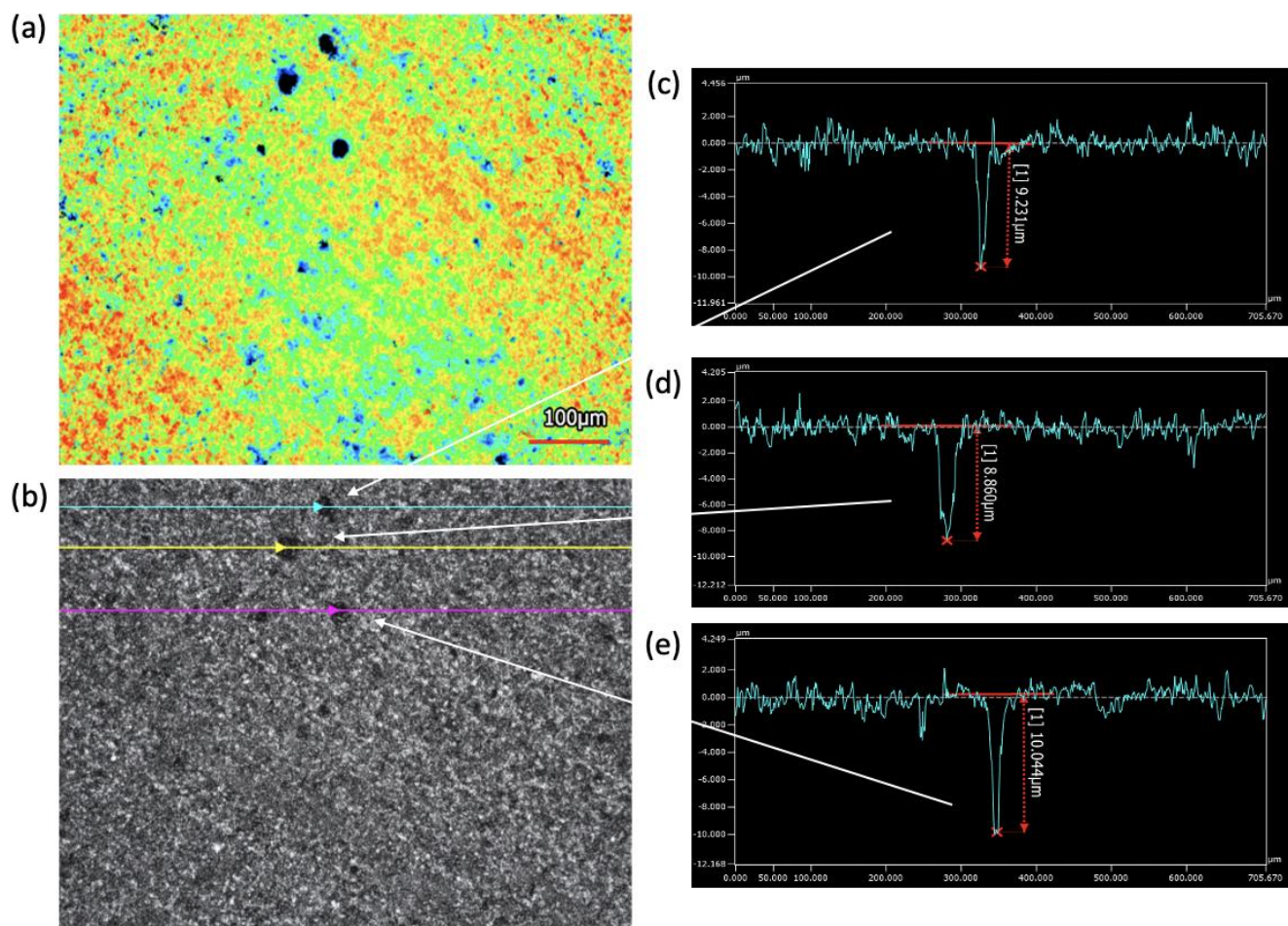


**Figure 4.7.** (a) Topographic image of a 1x1 mm<sup>2</sup> sample at 20x magnification on the surface of the solid electrolyte disc (b) further analysis of large divots found (c) topmost divot from (b) with a depth of 9.231 microns (d) midrange divot from (b) with a depth of 8.860 microns (e) bottommost divot from (b) with a depth of 10.044 microns.

As shown, there are various pits throughout the electrolyte surface. The area surrounding these pits have an average peak-to-valley height of greater than 1 micron. The sampling was random, and as such, it cannot be posited that the imaged pits are the only ones on the NBA surface. The deposited rectangular sodium pads were of a five-micron thickness, meaning these dips were nearly twice the depth of the electrodes. This would lead to poor contact between the deposited electrodes and

electrolyte and would introduce uncertainty when using the micromanipulators as probes. After this determination, a new configuration was determined, as described in Section 4.2.1.

#### 4.3.3 Application of Pressure

As in the initial test with the through-plane symmetric cell, we first sought proof of cyclability with our in-plane cells. As such, low current density was explored due to expected failure at  $0.5 \text{ mA cm}^{-2}$  with no applied pressure.<sup>40</sup> Cycling was performed from 5 to  $50 \text{ } \mu\text{A}$  and the resulting voltage was expected at low currents.

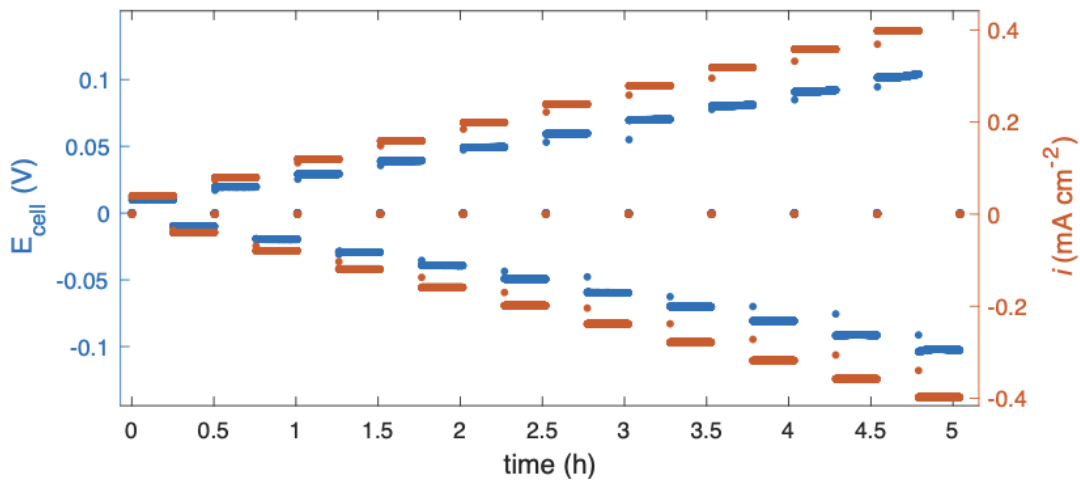


**Figure 4.8.** Cycling data of the symmetric in-plane cell without applied load. In this test, the current density ranged from  $0.04$  to  $0.4 \text{ } \mu\text{A cm}^{-2}$ . Current was increased stepwise in 20-minute increments with a short (2 minutes) rest step between each constant current application.. This suggests that interfacial contact between the electrode and electrolyte is sufficient.

Again, cycling at low current density ( $0.04$  to  $0.4 \text{ mA cm}^{-2}$ ) proved successful, as shown in Figure 4.8. However, it should be noted that the voltage response began to behave unexpectedly at  $0.4 \text{ mA cm}^{-2}$ . A slight increased initial resistance is

observable, though modest. This is similar to findings from the through-plane symmetric cell.

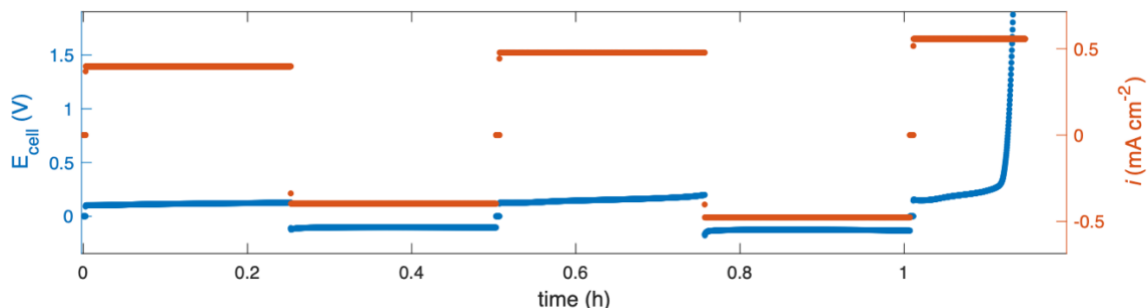


**Figure 4.9.** Stepwise increase from  $0.4 \mu\text{A cm}^{-2}$  to  $0.55 \mu\text{A cm}^{-2}$  (red). Cell resistance increases significantly at  $0.55 \mu\text{A cm}^{-2}$ , as depicted by the voltage response (blue)

As shown in Figure 4.9, the voltage response increased at higher current densities. This was expected, as there was no applied pressure. This increased resistance is likely due to interfacial interactions, or lack thereof. Void formation was suspected, and as such, external pressure was applied and cycling was resumed. It was observed that even after a pair of sodium pads experienced a dramatic increase of resistance (Figure 4.9), applying load to one electrode allowed for continued cyclability at a low current density, as shown in Figure 4.10a.

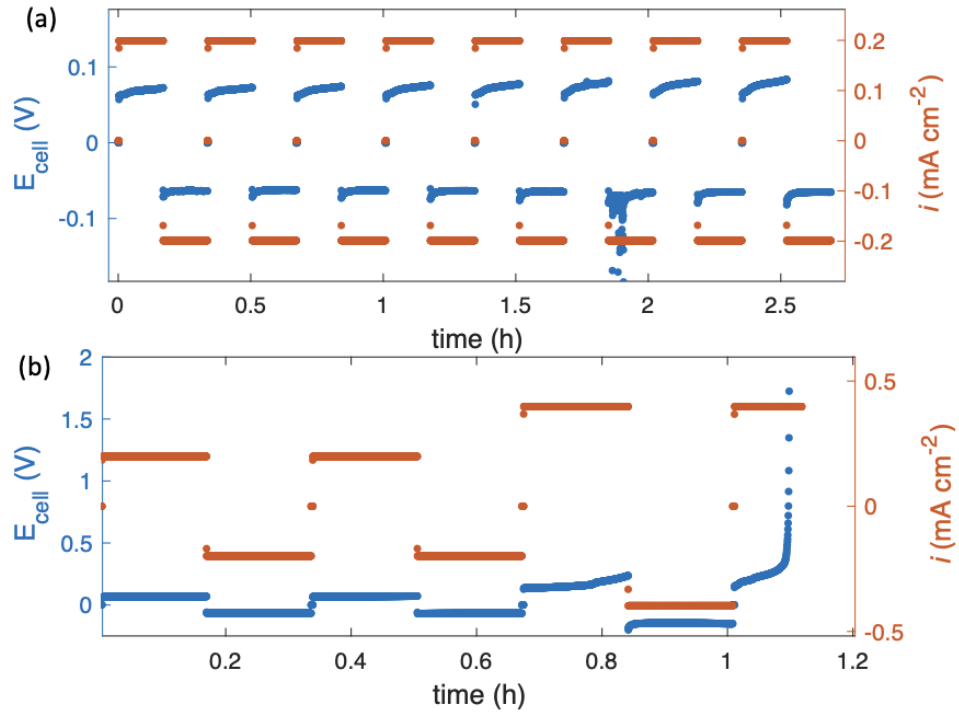


**Figure 4.10.** (a) Consistent cycling at a current densities of  $0.2 \text{ mA cm}^{-2}$  under approx. 8MPa. (b) Stepwise increase of current from  $0.2$  to  $0.4 \text{ mA cm}^{-2}$ .

This is interesting to us, as the load was applied to the electrode that had last been stripped. Thus, the pressure likely improved the interfacial contact between the electrode and electrolyte. We observed a modest increase of voltage as cycle number increased. However, stepping the current density to  $0.4 \text{ mA cm}^{-2}$  proved to incite a spike in resistance. This could be attributed to using a cell that had been previously cycled and the load application, as the second electrode did not benefit from increased interfacial contact.

#### 4.4 Conclusions

The work presented in this chapter shows the promise of investigating in-plane cells. This approach is novel in research regarding solid state batteries featuring thin-film sodium anodes. As such, conclusions made here should be verified in future experiments.

While other works have used SEM to observe surface defects of ceramic electrolytes, we found SEM is not adequate for thin-film applications. By employing a confocal microscope, the surface roughness was found to be greater than 5 microns. While this may be a reasonable roughness for crude sodium ingot application, this is simply too rough for viable thin film deposition, as the electrodes were thinner than the surface divots.

Pressure has been shown to increase cyclability of cells, as seen with through-plane symmetric cells. However based on our findings, applying pressure to only one electrode is not sufficient.

## Chapter 5: Conclusions and Recommendations

### 5.1 Conclusions

We determined appropriate materials by conducting a search through the literature to obtain a miniature review before beginning experimental work. Through our literary findings and experimental work, we can conclude the following:

- (1) A thorough review into the literature shows that significant work has been done to address the challenges of metal anodes in solid-state batteries. However, inconsistent parameterization for testing procedures makes an accurate comparison of the data difficult. To effectively investigate novel materials and treatments and better understand the complex phenomena occurring at the solid electrolyte/anode interface, easily comparable testing protocols is are crucial.
- (2) The solid electrolyte should undergo adequate surface treatments to decrease unnecessary interfacial resistance immediately prior to testing. We found that a 850°C heat treatment for only 2 hours is sufficient, compared to a 12-hour treatment, allowing for more efficient use of time and resources. However, it should be noted that heat treatment is only one of various steps taken to reduce interfacial resistance. Further treatment to the electrolyte and electrodes to account for the interactions at the surface.
- (3) Ensuring the application of constant pressure reduces uncertainty in the testing setup. While keeping constant pressure did not seem to have a significant effect on resistance, it was possible to better understand the issues at the interface.. While the mechanism behind rising interfacial resistance upon cycling is not well understood,

confidence in the methodology and resulting data is of utmost importance. It is postulated that the increased resistance is due to oxidation of the electrolyte, void formation, or surface interactions between the electrode and electrolyte. Further testing must be done to better understand the interfacial chemistries.

(4) In the in-plane cell, as it was possible to cycle a cell that had previously reached significant resistance by applying a load. This suggests that pressure is an important factor in preventing rising resistance as a function of cycle number, specifically that applying pressure allows for increased cyclability. Further work must be done to better understand the exact interface interactions, but pressure likely extends the life of the cell by increasing sodium creep to the interface.

### 5.2 Recommendations for Future Work

Sodium is a desirable anode material but proves difficult to manage. Its mechanical properties and reactivity present challenges in cell assembly and at the interface. Based on our conclusions in Section 5.1, possible directions to streamline future research are presented here.

(1) For the through-plane cell, the current setup needs improvement. It would benefit from a masking procedure to maintain a defined, constant active area. The mask would both ensure alignment of the electrodes and prevent sodium creep from affecting the test. Misaligned electrodes introduce unnecessary nonuniform current densities. Meanwhile, disassembling the jig and remeasuring the electrode areas results in excessive handling which can introduce opportunities for the cell to be dropped, crushed, or otherwise physically compromised. Even after the electrode area

has been measured, the sodium will continue to creep under pressure, which can cause an area mismatch in electrodes, also unnecessarily compromising current density uniformity. Further, an area with a moving boundary causes inconsistencies in area-specific resistance, current density, and cycling calculations. It should be emphasized that the mask/electrolyte interface must not allow sodium creep beneath the mask. The mask should not rely on pressure to maintain this intimate interface, as that will disrupt the measured stack pressure on the cell. A standardized process will allow for more confidence in the tests, increase efficiency of the testing process, and better comparison of results.

(2) For both in-plane and through-plane cells, incorporating a reference electrode is necessary to differentiate between electrodes due to electrode symmetry. Thus, a three-electrode setup should be considered and pursued. Though sodium would be an ideal reference electrode, employing alloys may prove more efficient due to sodium's reactivity. Further research should be done to investigate which, if any, sodium alloys will be most appropriate for the reference electrode. Modeling work could prove invaluable for determining optimal electrode materials, placement, and dimensions.

(3) For the in-plane cell, a smoother solid electrolyte must be pursued. The commercial roughness of the NBA discs is significant and continued use of this electrolyte requires wet-polishing to the sub-micron level for thin-film applications. Further research should be done to better understand the effects of grain boundaries and surface chemistry on the cell, especially on the thin-film scale. Alternatively, other electrolytes with low surface roughness or well-understood sodium interactions can be investigated.

(4) While symmetric cells give useful insights, they are impractical and full cell work is crucial to better understanding of interactions among the electrolyte and electrodes. Thus, full cells employing solid-state electrolytes, a sodium metal anode, and corresponding cathode should be considered and researched.

## Bibliography

1. US EPA, O. Sources of Greenhouse Gas Emissions.  
<https://www.epa.gov/ghgemissions/sources-greenhouse-gas-emissions> (2015).
2. US EPA, O. Overview of Greenhouse Gases.  
<https://www.epa.gov/ghgemissions/overview-greenhouse-gases> (2015).
3. Rowlatt, J. Why electric cars will take over sooner than you think. *BBC News* (2021).
4. U.S. Energy System Factsheet | Center for Sustainable Systems.  
<https://css.umich.edu/factsheets/us-energy-system-factsheet>.
5. Wang, M. J., Carmona, E., Gupta, A., Albertus, P. & Sakamoto, J. Enabling “lithium-free” manufacturing of pure lithium metal solid-state batteries through in situ plating. *Nat. Commun.* **11**, 5201 (2020).
6. Scrosati, B. History of lithium batteries. *J. Solid State Electrochem.* **15**, 1623–1630 (2011).
7. Schipper, F. & Aurbach, D. A brief review: Past, present and future of lithium ion batteries. *Russ. J. Electrochem.* **52**, 1095–1121 (2016).
8. Cheng, X.-B., Zhang, R., Zhao, C.-Z. & Zhang, Q. Toward Safe Lithium Metal Anode in Rechargeable Batteries: A Review. *Chem. Rev.* **117**, 10403–10473 (2017).
9. Hou, W. *et al.* Solid electrolytes and interfaces in all-solid-state sodium batteries: Progress and perspective. *Nano Energy* **52**, 279–291 (2018).
10. Seh, Z. W., Sun, J., Sun, Y. & Cui, Y. A Highly Reversible Room-Temperature Sodium Metal Anode. *ACS Cent. Sci.* **1**, 449–455 (2015).

11. Cohn, A. P., Muralidharan, N., Carter, R., Share, K. & Pint, C. L. Anode-Free Sodium Battery through in Situ Plating of Sodium Metal. *Nano Lett.* **17**, 1296–1301 (2017).
12. Oh, J. A. S., He, L., Chua, B., Zeng, K. & Lu, L. Inorganic sodium solid-state electrolyte and interface with sodium metal for room-temperature metal solid-state batteries. *Energy Storage Mater.* **34**, 28–44 (2021).
13. Kerman, K., Luntz, A., Viswanathan, V., Chiang, Y.-M. & Chen, Z. Review—Practical Challenges Hindering the Development of Solid State Li Ion Batteries. *J. Electrochem. Soc.* **164**, A1731–A1744 (2017).
14. U.S. Geological Survey, 2021, *Mineral Commodity Summaries: Lithium*. doi:<https://doi.org/10.3133/mcs2021>. (2021).
15. Bolen, W. P. U.S. Geological Survey, 2021, *Mineral Commodity Summaries: Soda Ash*. doi:<https://doi.org/10.3133/mcs2021>. (2021).
16. Kim, H. *et al.* Recent Progress in Electrode Materials for Sodium-Ion Batteries. *Adv. Energy Mater.* **6**, 1600943 (2016).
17. Lee, B., Paek, E., Mitlin, D. & Lee, S. W. Sodium Metal Anodes: Emerging Solutions to Dendrite Growth. *Chem. Rev.* (2019) doi:10.1021/acs.chemrev.8b00642.
18. Lu, X. *et al.* Liquid-metal electrode to enable ultra-low temperature sodium-beta alumina batteries for renewable energy storage. *Nat. Commun.* **5**, 1–8 (2014).
19. Baclig, A. C. *et al.* High-Voltage, Room-Temperature Liquid Metal Flow Battery Enabled by Na-K|K- $\beta$ '-Alumina Stability SI. *Joule* **2**, 1287–1296 (2018).

20. Zhao, Q., Stalin, S., Zhao, C.-Z. & Archer, L. A. Designing solid-state electrolytes for safe, energy-dense batteries. *Nat. Rev. Mater.* **5**, 229–252 (2020).
21. Ma, Q. *et al.* A new Na[(FSO<sub>2</sub>) (n-C<sub>4</sub>F<sub>9</sub>SO<sub>2</sub>)N]-based polymer electrolyte for solid-state sodium batteries. *J. Mater. Chem. A* **5**, 7738–7743 (2017).
22. Qi, X. *et al.* Sodium Bis(fluorosulfonyl)imide/Poly(ethylene oxide) Polymer Electrolytes for Sodium-Ion Batteries. *ChemElectroChem* **3**, 1741–1745 (2016).
23. Fergus, J. W. Ceramic and polymeric solid electrolytes for lithium-ion batteries. *J. Power Sources* **195**, 4554–4569 (2010).
24. Zheng, Y. *et al.* High-Capacity All-Solid-State Sodium Metal Battery with Hybrid Polymer Electrolytes. *Adv. Energy Mater.* **8**, 1801885 (2018).
25. Krauskopf, T., Richter, F. H., Zeier, W. G. & Janek, J. Physicochemical Concepts of the Lithium Metal Anode in Solid-State Batteries. *Chem. Rev.* **120**, 7745–7794 (2020).
26. Lu, X., Xia, G., Lemmon, J. P. & Yang, Z. Advanced materials for sodium-beta alumina batteries: Status, challenges and perspectives. *J. Power Sources* **195**, 2431–2442 (2010).
27. Lu, X. *et al.* Liquid-metal electrode to enable ultra-low temperature sodium-beta alumina batteries for renewable energy storage. *Nat. Commun.* **5**, 4578 (2014).
28. Randau, S. *et al.* Benchmarking the performance of all-solid-state lithium batteries. *Nat. Energy* **5**, 259–270 (2020).
29. Taylor, N. J. *et al.* Demonstration of high current densities and extended cycling in the garnet Li<sub>7</sub>La<sub>3</sub>Zr<sub>2</sub>O<sub>12</sub> solid electrolyte. *J. Power Sources* **396**, 314–318 (2018).

30. Fincher, C. D., Zhang, Y., Pharr, G. M. & Pharr, M. Elastic and Plastic Characteristics of Sodium Metal. *ACS Appl. Energy Mater.* **3**, 1759–1767 (2020).
31. Kasemchainan, J. *et al.* Critical stripping current leads to dendrite formation on plating in lithium anode solid electrolyte cells. *Nat. Mater.* **18**, 1105–1111 (2019).
32. Schmuch, R., Wagner, R., Hörpel, G., Placke, T. & Winter, M. Performance and cost of materials for lithium-based rechargeable automotive batteries. *Nat. Energy* **3**, 267–278 (2018).
33. Weiss, M. *et al.* From Liquid- to Solid-State Batteries: Ion Transfer Kinetics of Heteroionic Interfaces. *Electrochem. Energy Rev.* **3**, 221–238 (2020).
34. Yu, Y., Xu, H., Wang, Z. & Shao, G. Transport of Sodium Ions in Solids: Progress in First-Principle Theoretical Formulation of Potential Solid Sodium-Ion Electrolytes. *Batter. Supercaps* **4**, 1096–1107 (2021).
35. Whittingham, M. S. & Huggins, R. A. Measurement of Sodium Ion Transport in Beta Alumina Using Reversible Solid Electrodes. *J. Chem. Phys.* **54**, 414–416 (1971).
36. *Ionotec Beta Alumina Ceramic Specification.*
37. Briant, J. L. & Farrington, G. C. Ionic Conductivity in Lithium and Lithium-Sodium Beta Alumina. *J. Electrochem. Soc.* **128**, 1830–1834 (1981).
38. Fertig, M. P. *et al.* From High- to Low-Temperature: The Revival of Sodium-Beta Alumina for Sodium Solid-State Batteries. *Batter. Supercaps* batt.202100131 (2021) doi:10.1002/batt.202100131.

39. Sharafi, A. *et al.* Surface Chemistry Mechanism of Ultra-Low Interfacial Resistance in the Solid-State Electrolyte  $\text{Li}_7\text{La}_3\text{Zr}_2\text{O}_{12}$ . *Chem. Mater.* **29**, 7961–7968 (2017).
40. Spencer Jolly, D. *et al.* Sodium/Na  $\beta''$  Alumina Interface: Effect of Pressure on Voids. *ACS Appl. Mater. Interfaces* **12**, 678–685 (2020).
41. Kasemchainan, J. & Bruce, P. G. All-Solid-State Batteries and their Remaining Challenges. *Johns. Matthey Technol. Rev.* **62**, 177–180 (2018).
42. Doux, J. *et al.* Stack Pressure Considerations for Room-Temperature All-Solid-State Lithium Metal Batteries. *Adv. Energy Mater.* **10**, 1903253 (2020).
43. Wang, M. J., Choudhury, R. & Sakamoto, J. Characterizing the Li-Solid-Electrolyte Interface Dynamics as a Function of Stack Pressure and Current Density. *Joule* **3**, 2165–2178 (2019).
44. Bay, M. *et al.* Sodium Plating from Na- $\beta''$ -Alumina Ceramics at Room Temperature, Paving the Way for Fast-Charging All-Solid-State Batteries. *Adv. Energy Mater.* **10**, 1902899 (2020).
45. Bay, M.-C. *et al.* Impact of sintering conditions and zirconia addition on flexural strength and ion conductivity of Na- $\beta''$ -alumina ceramics. *Mater. Today Commun.* **23**, 101118 (2020).
46. Kim, Y., Ha, K.-H., Oh, S. M. & Lee, K. T. High-Capacity Anode Materials for Sodium-Ion Batteries. *Chem. - Eur. J.* **20**, 11980–11992 (2014).
47. Xie, J. & Lu, Y.-C. A retrospective on lithium-ion batteries. *Nat. Commun.* **11**, 2499 (2020).

48. Sun, B. *et al.* Design Strategies to Enable the Efficient Use of Sodium Metal Anodes in High-Energy Batteries. *Adv. Mater.* **32**, 1903891 (2020).
49. Kazyak, E. *et al.* Li Penetration in Ceramic Solid Electrolytes: Operando Microscopy Analysis of Morphology, Propagation, and Reversibility. *Matter* **2**, 1025–1048 (2020).
50. Ning, Z. *et al.* Visualizing plating-induced cracking in lithium-anode solid-electrolyte cells. *Nat. Mater.* **20**, 1121–1129 (2021).
51. Flatscher, F., Philipp, M., Ganschow, S., Wilkening, H. M. R. & Rettenwander, D. The natural critical current density limit for  $\text{Li}_7\text{La}_3\text{Zr}_2\text{O}_{12}$  garnets. *J. Mater. Chem. A* **8**, 15782–15788 (2020).